

# Nonvolatile Rewritable Photomemory Arrays Based on Reversible Phase-Change Perovskite for Optical Information Storage

Chen Zou, Jiajiu Zheng, Cheng Chang, Arka Majumdar, and Lih Y. Lin\*

The high transmission speed of optical signals and their application in optical computation have created a growing demand for photon-programmed memory devices. Rather than using electrical pulses to store data in one of two states, the photomemory (PM) devices exploit the optical stimulation to store the light information. In this work, the application of a nonvolatile rewritable PM array using the photochromic inorganic perovskite CsPbIBr<sub>2</sub> grown by a vapor-deposition process is demonstrated. Reversible phase transitions between orthorhombic ( $\delta$ ) and cubic ( $\alpha$ ) phases are achieved in CsPbIBr<sub>2</sub> films through laser-induced heat and moisture exposure. The PM pixels in an optically absorbing perovskite phase exhibit  $\approx 50$ -fold photoresponsivity as large as those in a transparent-colored non-perovskite phase. Storing optical data are achieved by heating pixels through a near-infrared laser, while moisture exposure is used to erase the stored information. The nonvolatile PM array exhibits great write-read-erase cycle endurance and data retention capability without obvious performance degradation after storage in air for one week. This work demonstrates the promising application of vapor-deposited inorganic perovskite for optical information storage and the unique potential of them for use in optical switches, tunable metasurfaces, and many other applications.

## 1. Introduction

The widespread application of optical fibers for optical signal transmission and the ongoing development of high-speed optical computing have created a growing need for developing light-writing memories.<sup>[1,2]</sup> Compared to conventional electrically programmed memories, photomemory devices adopt the photon-programming and store the light information instead, which is an essential block for optical data processing and photonic computation circuits.<sup>[3,4]</sup> In addition, photomemory

Dr. C. Zou, Dr. J. Zheng, Dr. C. Chang, Prof. A. Majumdar, Prof. L. Y. Lin  
Department of Electrical and Computer Engineering  
University of Washington  
Seattle, WA 98195, USA  
E-mail: lylin@uw.edu

Prof. A. Majumdar  
Department of Physics  
University of Washington  
Seattle, WA 98195, USA

 The ORCID identification number(s) for the author(s) of this article can be found under <https://doi.org/10.1002/adom.201900558>.

DOI: 10.1002/adom.201900558

devices combine both functions of photosensors and memories, and thus simplify the device structure by eliminating the demand for additional memory components to store the output of the photosensors.<sup>[5]</sup>

Recently, metal halide perovskite has attracted much research interest due to its outstanding optoelectronic properties including exceptional optical absorption, high carrier mobility, and long carrier lifetime.<sup>[6,7]</sup> These characteristics have promoted its fast development in photosensing devices including photovoltaics,<sup>[8]</sup> photodetectors,<sup>[9–11]</sup> and phototransistors.<sup>[12]</sup> However, most of these perovskite photosensing devices only convert the light illumination to transient electrical signals, requiring another processing component to store the output signals for recording light information. More recently, perovskite-based photon-programmed memory was developed using the floating-gate transistor architecture.<sup>[13,14]</sup> However, these memory behaviors relied on the trapping of photoinduced charges in the perovskite surrounded by insulating polymer matrix, which could not last for a long time (1000 s).

In this work, we utilized the photochromic all-inorganic perovskite CsPbIBr<sub>2</sub> to demonstrate a nonvolatile, rewritable, photon-programmed memory array for optical information storage.

The photomemory (PM) pixel is composed of an Ag interdigitated electrode (IDE) and vapor-deposited perovskite film atop. The reversible phase transitions of vapor-deposited CsPbIBr<sub>2</sub> films between the perovskite (PVSK) phase and non-perovskite (non-PVSK) phase were achieved through laser heating/moisture exposure cycles. The two different phases correspond to significant distinctions in optoelectronic properties including photoluminescence (PL), optical absorption, refractive index, charge transport, etc.<sup>[15,16]</sup> Instead of heating all PM pixels together on a heater platform, a Nd:YVO<sub>4</sub> laser ( $\lambda = 1064$  nm) was used to generate heat selectively in specific PM pixels through the photo-thermal effect in Ag,<sup>[17]</sup> which made the transition from the non-PVSK to PVSK phase site-selectable. The PM pixel in the PVSK phase showed a high responsivity up to 1.5 A W<sup>-1</sup> with a broad absorption spectrum from 350 to 600 nm.

On the contrary, the PM pixel in the non-PVSK phase exhibits a much smaller photoresponsivity and a narrower absorption spectrum. Such a large difference in PM performance enabled the laser heating and moisture exposure to “set” and “reset” the selected PM pixels, and the photocurrents are read out to extract the phase information written by laser irradiation. Our PM pixels exhibited great stability over ten write-read-erase cycles without significant performance degradation. Furthermore, the PM pixels could keep the phase information after being stored in ambient condition (30–40% humidity) for one week.

## 2. Results and Discussion

### 2.1. Characterization of Vapor-Deposited CsPbIBr<sub>2</sub> Thin Films

In this study, we used CsPbIBr<sub>2</sub> in further characterizations and device fabrication due to its better stability. The fabrication procedure of the vapor-deposited CsPbIBr<sub>2</sub> PM array is schematically illustrated in Figure 1a. The glass substrate was first ultrasonically cleaned and placed onto a printing platform. Conductive silver ink was then inkjet-printed onto the substrate to form an 8 × 8 IDE array (see the Experimental Section). The CsPbIBr<sub>2</sub> film was deposited onto the prepatterned substrate via a vapor-deposition process. The CsI and PbBr<sub>2</sub> were separately placed into two crucibles and simultaneously sublimed. By controlling the evaporation rates of the two sources, the mixed halide inorganic CsPbIBr<sub>2</sub> films can be obtained. Figure S1 (Supporting Information) shows the element distribution of

iodide (I) and bromide (Br), the I/Br molar ratio maintains ≈1:2 along the feature line, indicating the formation of the CsPbIBr<sub>2</sub> thin film.

The top-view scanning electron microscopy (SEM) image of the CsPbIBr<sub>2</sub> film is presented in Figure 1b. The homogeneous CsPbIBr<sub>2</sub> film shows complete surface coverage without obvious pinholes (see Figure S2, Supporting Information, for more SEM images in details). The atomic force microscopy (AFM) image of the CsPbIBr<sub>2</sub> film in Figure 1c shows the surface roughness of 4.1 nm in a typical area of 5 × 5 μm<sup>2</sup>, smaller than that of spin-coated film (Figure S3, Supporting Information), further confirming the flat and smooth surface morphology. A unique advantage of the vapor deposition over solution-cast process is that patterned perovskite thin films can be readily achieved through a shadow mask and more compatible with flexible substrates. A dot array pattern made of vapor-deposited CsPbIBr<sub>2</sub> on a flexible polyethylene terephthalate (PET) substrate is clearly observed in Figure 1d.

### 2.2. Phase Transitions of Inorganic Perovskites via Heating and Moisture Exposure

As shown in Figure 2a, the as-deposited CsPbIBr<sub>2</sub> film (PVSK phase) displayed an orange-red color. The synthesized CsPbIBr<sub>2</sub> film could maintain its color in an inert or low humidity (<40%) environment. Lin et al. have reported the reversible phase transition of solution-cast CsPbI<sub>x</sub>Br<sub>3-x</sub> films between the room-temperature non-PVSK phase and high-temperature PVSK phase.<sup>[18]</sup> However, CsPbI<sub>x</sub>Br<sub>3-x</sub> is much less soluble in

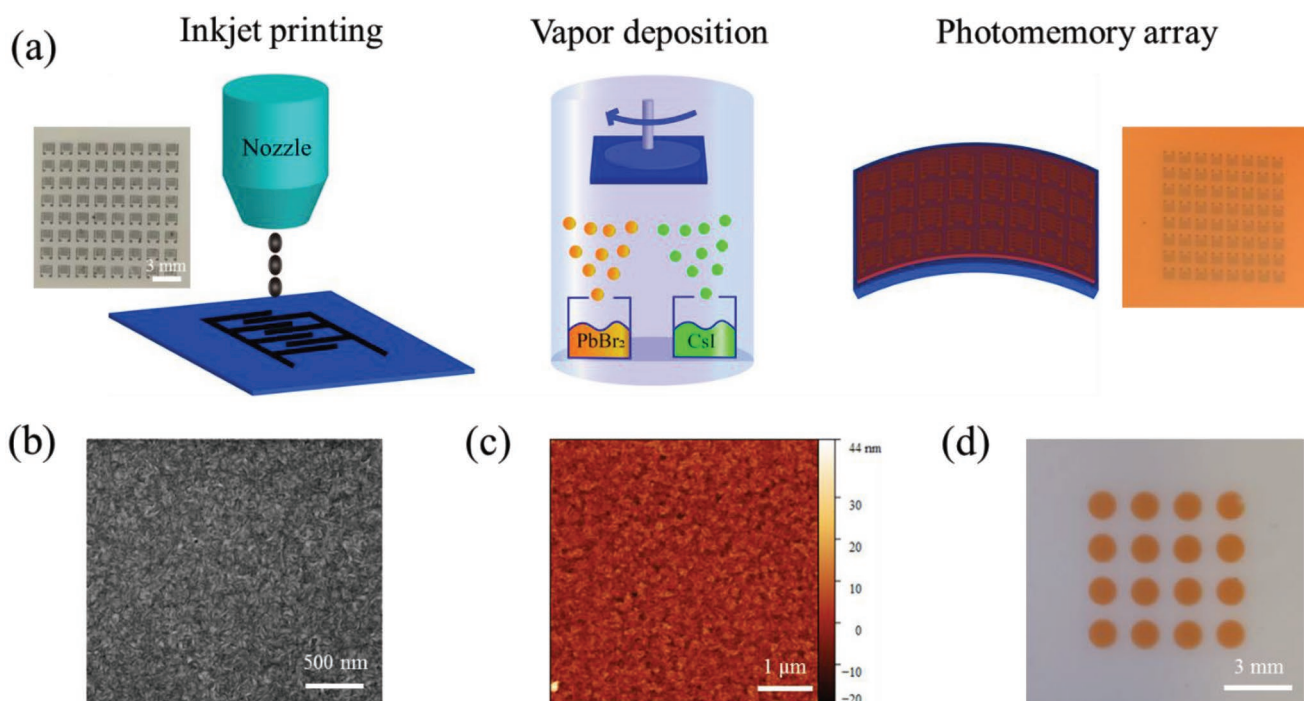


**Figure 1.** Fabrication and characterization of all-inorganic CsPbIBr<sub>2</sub> perovskite thin films. a) The schematic fabrication procedure of all-inorganic perovskite PM array via inkjet printing technology and dual-source thermal vapor deposition method. b) The SEM image of the CsPbIBr<sub>2</sub> film with a scale bar of 500 nm. c) The AFM image of the CsPbIBr<sub>2</sub> film, the RMS roughness is 4.1 nm. d) The optical image of a vapor-deposited perovskite dot array on a flexible PET substrate patterned through a shadow mask.

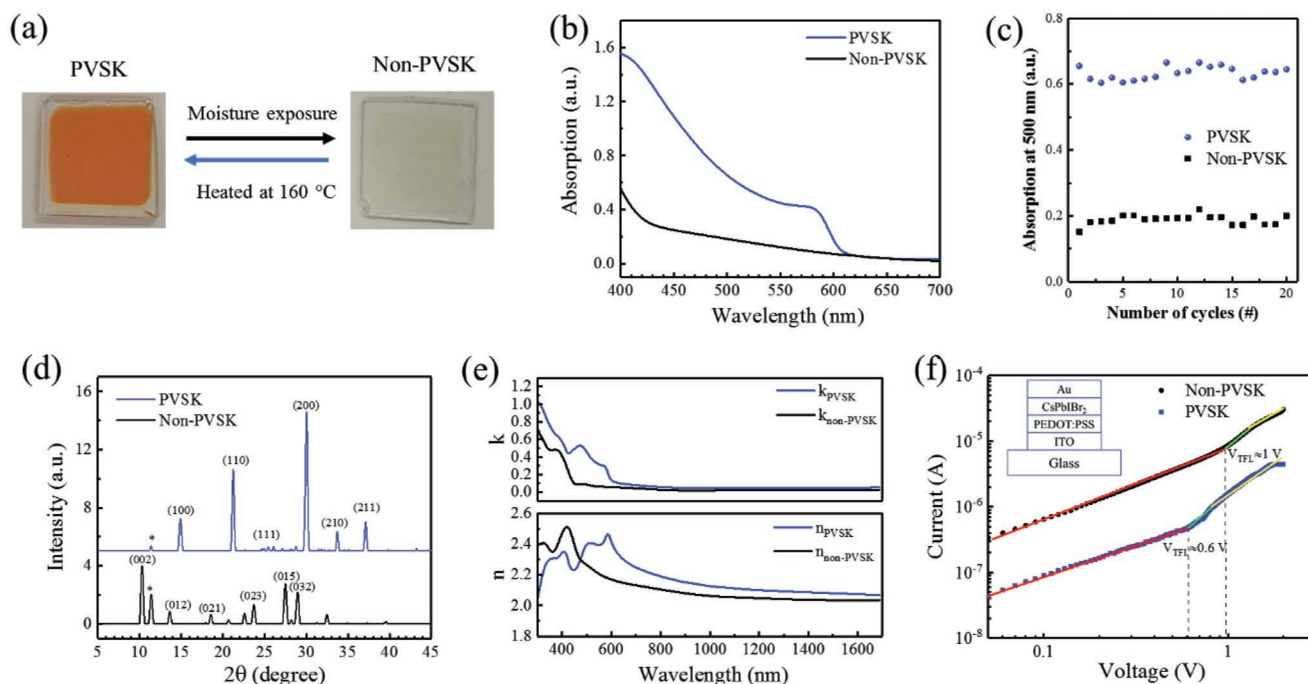


**Figure 2.** Phase transitions of inorganic perovskite thin films via laser heating and moisture exposure, taking CsPbI<sub>2</sub> for example. a) Optical images of PVSK (orange-red color) and non-PVSK phase (transparent) CsPbI<sub>2</sub> thin films. The reversible phase transitions can be achieved by heating/moisture exposure. b) The absorption spectra of PVSK and non-PVSK CsPbI<sub>2</sub> films. c) The reversible and repeatable switching behavior of the absorption (at 500 nm) of the CsPbI<sub>2</sub> thin film over 20 phase transition cycles. d) XRD patterns and e) complex refractive index spectra of PVSK and non-PVSK CsPbI<sub>2</sub> films. f) *I*-*V* curves of hole-only devices (ITO/PEDOT:PSS/CsPbI<sub>2</sub>/Au) where the CsPbI<sub>2</sub> layer is either in the non-PVSK or PVSK phase. The *I*-*V* curve is fitted by  $I \approx V^n$ ; the red, green, and yellow fitting line represents  $n = 1$ ,  $n > 2$ , and  $n = 2$ , respectively.

solutions, which limits its applications in solution-processed optoelectronic devices.<sup>[19]</sup> On the other hand, the vapor-deposition method offers many advantages including good film morphology, precisely controlled thickness, ease of patterning, high reproducibility, and better adaptability in flexible device fabrications.<sup>[20,21]</sup> In this work, we observed a similar phenomenon in the vapor-deposited CsPbI<sub>2</sub> film as reported by Lin and co-workers. After exposed to an atmosphere with 80% relative humidity for 20 min, the orange-red CsPbI<sub>2</sub> film gradually turned to be transparent. Reheating the transparent CsPbI<sub>2</sub> film (non-PVSK phase) around 160 °C in a N<sub>2</sub>-filled glove box triggered the color-change from transparent back to orange-red again. The reversible phase transition of CsPbI<sub>2</sub> is repeatable and the optical properties in both phases remained consistent after 20 cycles, as discussed below.

Figure 2b presents the absorption spectra of the non-PVSK and PVSK phase CsPbI<sub>2</sub> films, showing the latter have significantly stronger optical absorption. Furthermore, the PVSK phase film shows an absorption edge at around 600 nm, while this is blueshifted to 430 nm for the non-PVSK phase film. Such a distinction can be used to distinguish CsPbI<sub>2</sub> films in these two different phases (see Figure S4, Supporting Information, for the time evolution of absorption spectra when the PVSK phase film was exposed to moisture). Furthermore, the PVSK phase film has longer PL lifetime than that of the non-PVSK phase film (Figure S5, Supporting Information). The reversibility of structural transitions between non-PVSK and PVSK phases was monitored by measuring the absorption spectra after repetitive moisture exposure and heating. Figure 2c shows

the absorption of CsPbI<sub>2</sub> films in the two phases at 500 nm. The data exhibit good consistency over 20 repetitive moisture/heat treatment cycles.

The X-ray diffraction (XRD) technique was used to analyze the crystal structural change in more details (Figure 2d). We notice that the PVSK phase CsPbI<sub>2</sub> film exhibits characteristic peaks located at 14.86°, 21.24°, and 30.0°, corresponding to the (100), (110), and (200) planes of  $\alpha$ -CsPbI<sub>2</sub>. This confirms that PbBr<sub>2</sub> and CsI layers have reacted to form one cubic-phase perovskite layer through an interdiffusion process. We also observe a small peak (denoted by \*) located at 11.4°, indicative of the remaining PbBr<sub>2</sub>, which is similar to the finding from Hutter et al.<sup>[22]</sup> The XRD pattern of the moisture-exposed CsPbI<sub>2</sub> film displays main peaks at 10.3°, 13.7°, 18.6°, 23.6°, 27.6°, and 28.8°, corresponding to (002), (012), (021), (023), (015), and (032) planes of  $\delta$ -CsPbI<sub>2</sub>.<sup>[23]</sup> Furthermore, we compared the XRD patterns of CsPbI<sub>2</sub> films in the two phases before and after phase-transition cycles (Figure S6, Supporting Information). No obvious difference was observed for both phases after 20 cycles.

The different crystal structures of CsPbI<sub>2</sub> films in non-PVSK and PVSK phases also result in a noticeable difference in refractive index. We measured the complex refractive index using an ellipsometry. Figure 2e shows the real part (*n*) and imaginary part (*k*) of the complex refractive index of non-PVSK and PVSK phase CsPbI<sub>2</sub> films. The *k* value of the PVSK phase film is almost zero after 600 nm, indicating no optical loss for  $\lambda > 600$  nm. In contrast, the *k* value of the non-PVSK phase film cuts off at  $\approx 430$  nm. These results are

consistent with the bandgap and absorption spectra in Figure 2b. The large difference of refractive index between two phases in the visible light region may have potential applications in optical modulators, switches, tunable metasurfaces, and other photonic devices.<sup>[24,25]</sup> Figure 2f presents the current–voltage ( $I$ - $V$ ) characteristics of a hole-only device (indium tin oxide (ITO)/poly(3,4-ethylenedioxythiophene) polystyrene sulfonate (PEDOT:PSS)/CsPbIBr<sub>2</sub>/Au); the CsPbIBr<sub>2</sub> layer is either in the non-PVSK or PVSK phase. Both  $I$ - $V$  curves ( $I \approx V^n$ ) show the ohmic ( $n = 1$ ), trap filling ( $n > 2$ ), and child regions ( $n = 2$ ).<sup>[26]</sup> The trap-filled voltage ( $V_{\text{TFL}}$ ) of the non-PVSK phase film was higher than that of the PVSK phase film, indicating a higher trap density ( $n_{\text{trap}}$ ).<sup>[27,28]</sup> This may be attributed to the release of halide atoms and increase of halide vacancies caused by the interaction of water molecules with Pb atoms.<sup>[29,30]</sup>

### 2.3. The Patterned Non-PVSK to PVSK Phase Transition through Laser Direct Writing (LDW)

Considering current technological trends toward flexible and wearable devices, a robust processing method such as heating for large-area flexible substrates is becoming more and more important.<sup>[31]</sup> Laser heating is a promising candidate for such an application. Compared to other more common thermal heating methods, laser heating has the advantage of area-selective rapid heating and cooling, better compatibility with flexible substrates, and processing scalability.<sup>[32–34]</sup> In this work, we employed a near-infrared (NIR) (1064 nm, Nd:YVO<sub>4</sub>) laser for LDW of the non-PVSK phase CsPbIBr<sub>2</sub> film deposited on an interfacial layer (ITO or Ag). This method can precisely control the heating temperature and crystallization process without damage by the laser beam.<sup>[35]</sup> Figure 3a presents the schematic

configuration of the LDW experimental setup. The sample was placed on a XY translation stage and driven laterally, a 1064 nm laser beam was focused onto the sample and laterally scanned the non-PVSK phase CsPbIBr<sub>2</sub> film on ITO. Two orange-red stripes were formed as shown in the inset photo of Figure 3a, indicating an instantaneous transformation of non-PVSK to PVSK phase triggered by the laser beam.

Figure 3b displays the optical (top) and fluorescent (bottom) microscopy images of a LDW pattern on the perovskite film. The laser beam was focused into an  $\approx 50$   $\mu\text{m}$  spot and scanned to form patterns. The PL of the PVSK phase area is much stronger than that of the non-PVSK phase area, which is clearly manifested in these fluorescent images. Figure 3c presents the line-scan PL intensity of the microline array pattern in Figure 3b, demonstrating the uniform periodic fluorescence emitted from the PVSK phase microline array. Raman spectroscopy has high positional and spectral accuracy, it was used here to investigate the phase mapping of the LDW patterns. In Figure 3d, the top Raman spectrum (blue curve) corresponds to the microlines with strong red fluorescence. A prominent peak at 138  $\text{cm}^{-1}$  is observed, which is attributed to the PVSK phase.<sup>[36]</sup> On the other hand, Raman spectrum of the dark background area (bottom black curve) shows a redshifted and broader peak at 114  $\text{cm}^{-1}$ , which corresponds to the non-PVSK phase.<sup>[33]</sup> The Raman measurement finding matches well with other reported literature,<sup>[37–39]</sup> further demonstrating the phase transformation induced by LDW.

The COMSOL simulated temperature distribution around a NIR laser spot (1  $\mu\text{m}$  diameter) shown in Figure 3e clarifies the underlying mechanism of photothermal heating. The NIR laser beam is not absorbed by the perovskite layer due to its wavelength longer than the absorption edge, and the photothermal effect from the interfacial layer (ITO) contributes to

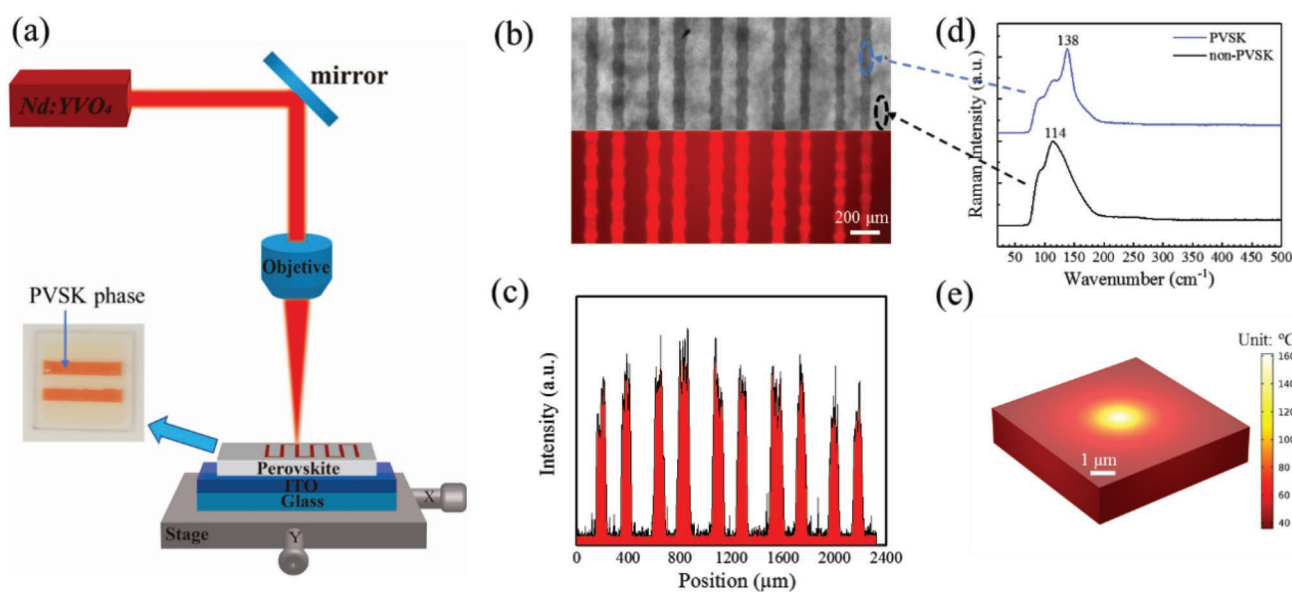


**Figure 3.** Laser direct writing (LDW) of the perovskite films assisted by photothermal effect. a) The schematic illustration for photothermal heating at the interfacial layer (ITO or Ag). The inset shows the photo of a perovskite thin film with two stripes converted to the PVSK phase through LDW. b) Optical (top) and fluorescent (bottom) microscopy images of the microlines pattern by LDW. c) The line-scan PL intensity of the fluorescent image in (b). d) The measured Raman spectra at different positions. The two distinct spectra correspond to the non-PVSK phase (black curve) and the PVSK phase (blue curve). e) COMSOL Multiphysics thermal simulation of heat distribution induced by a laser beam (9 mW) with a spot size of 1  $\mu\text{m}$ .

rapid local heating. A relative low laser power (9 mW) could lead a temperature rise of 160 °C localized to the focused beam position, which is hot enough to locally induce the phase transition. Around the focused laser spot, the temperature decreased to half of the maximum at a distance 1.4 μm from the center (see Figure S7, Supporting Information, for thermal simulation in details). The increased surface temperature as a function of laser intensity was measured using an IR thermal camera for both Ag and ITO as the interfacial layer (Figure S8, Supporting Information). The temperature rise strongly depends on the material of the interfacial layer, and it was observed that the Ag layer induced more photothermal heating and temperature rise than ITO at the same laser intensity. To induce phase transition from the non-PVSK to PVSK phase (160 °C), the laser intensity for Ag and ITO is ≈115 and ≈235 W cm<sup>-2</sup>, respectively.

#### 2.4. The Data Storage Mechanism of PMs Enabled by Nonvolatile Phase Transitions

The as-fabricated PVSK phase PM array was first exposed to water moisture with relative humidity of 80% until the perovskite film became transparent. As schematically illustrated in Figure 4a, one PM pixel was then heated by the focused laser beam selectively. The induced photothermal heating led to an instantaneous temperature rise at specific pixels, and a color change from transparent to orange-red was observed within a second. The inset photo in Figure 4a is a fluorescent image of one pixel heated by the laser beam. The uniform fluorescence

inside the IDE demonstrates the occurrence of phase transformation in that pixel. We noticed that the fluorescence is weaker directly on top of the Ag electrode area, which is attributed to PL quenching effect by Ag.

We then measured the current–voltage (*I*–*V*) curves of both non-PVSK and PVSK phase PM pixels in dark condition and under white light illumination (tungsten-halogen lamp), the results are presented in Figure 4b. PMs in two phases exhibit similar dark current (*I*<sub>dark</sub>) on the level of 10<sup>-9</sup> A at 5 V. The non-PVSK phase PM has slightly higher dark current, which may be attributed to the higher conductivity of non-PVSK phase films as shown in Figure 2f. Upon white light illumination, the photoinduced carriers contributed to the current increase of PMs in both phases. However, the light current (*I*<sub>light</sub>) of PMs in PVSK phase was ≈50 times larger than that of the PMs in non-PVSK phase when operated at a bias of 5 V. The large difference of photocurrents between PMs in two phases is attributed to the different crystal structures and optical absorptions. The responsivity (*R*), a key figure of merit for a PM, is given by<sup>[12]</sup>

$$R = \frac{I_{ph}}{E_e S} = \frac{I_{light} - I_{dark}}{E_e S} \quad (1)$$

where *E<sub>e</sub>* and *S* are the illumination intensity and the single PM device area, respectively. As shown in Figure 4c, a large difference of spectral responsivity between PMs in the two phases is observed. The responsivity spectrum shows a cutoff at 430 and 600 nm for the non-PVSK and PVSK phase PMs, respectively.

The *I*–*V* curves of the PVSK phase PMs under 405 nm irradiation with light intensity varying from 0 to 50 mW cm<sup>-2</sup> are

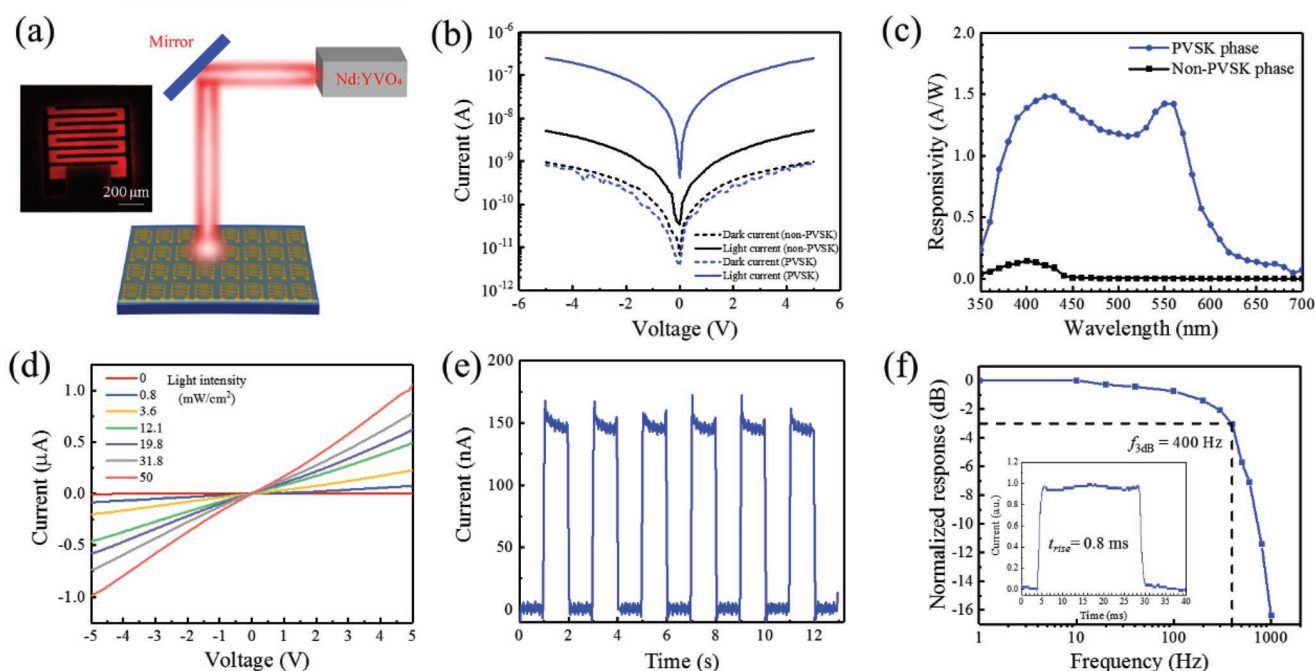


**Figure 4.** Detection performance of inorganic perovskite PMs. a) The schematic illustration of a single perovskite PM pixel heated by a 1064 nm laser. The inset photo is the fluorescent image of the pixel after transitioning to the PVSK phase. b) *I*–*V* curves of CsPbIBr<sub>2</sub> PM pixels in the non-PVSK phase and PVSK phase, under dark and white light illumination. c) The responsivity spectra of the perovskite PM pixel in two phases. d) *I*–*V* curves of the perovskite PM in the PVSK phase under 405 nm light illumination with different intensities. e) The time-dependent photocurrent switching behavior, and f) normalized frequency response of the PM in the PVSK phase. The inset shows the magnified photoresponse under 20 Hz light modulation.

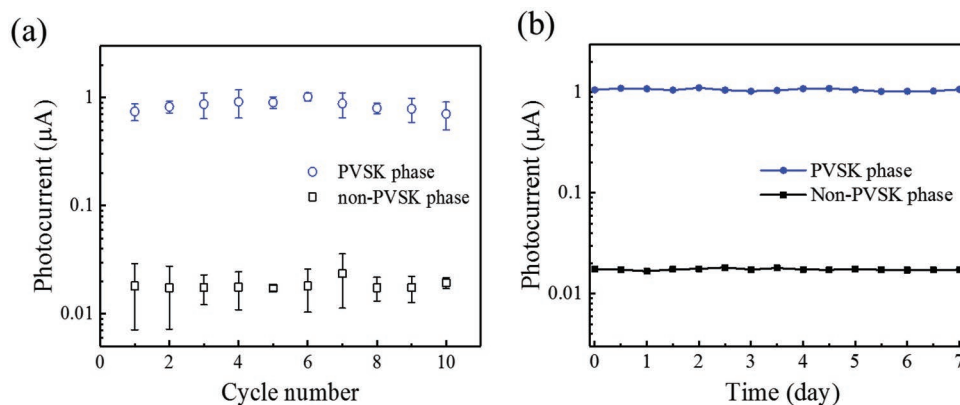


**Figure 5.** The data storage application enabled by the phase transition between the nonvolatile PVSK and non-PVSK phases. a) The photocurrents of perovskite PM pixels in PVSK and non-PVSK phases during ten cycles of laser heating/moisture exposure test. b) Data retention capability of the nonvolatile PVSK and non-PVSK phase perovskite PMs. There is no obvious degradation for the photocurrents in both phases after storage in air for one week under 30–40% relative humidity.

shown in Figure 4d, the current shows linear relationship with voltage. The linear dynamic range (LDR), representing the range of the incident light intensity over which the photoresponse is linear, was measured to be 63 dB (see Figure S9, Supporting Information, for the photocurrent dependence on the light intensity). The response speed is another key parameter for PMs. Figure 4e exhibits the time-dependent photocurrent response under periodically modulated UV light illumination. The PMs show stable and reproducible photoresponse behaviors under periodic on/off switching cycles. The rise time (defined as the time for the photocurrent to increase from 10 to 90% of the peak value) and the fall time (from 90 to 10% of the peak value) are extracted to be 0.8 and 1 ms (inset of Figure 4f), respectively. We then measured the 3 dB frequency bandwidth by recording photocurrent as a function of the modulated light frequency, as presented in Figure 4f. The 3 dB bandwidth  $f_{3dB}$  is found to be  $\approx 400$  Hz, which is consistent with theoretical value calculated by  $f_{3dB} = 0.35/t_{rise}$ . We also fabricated the perovskite PM array on a flexible substrate, the device exhibited good mechanical bending capability and could maintain its photoresponse performance after various bending cycles (Figure S10, Supporting Information).

As discussed above, the crystal structure difference between the two phases leads to dramatically different photoresponse under white light irradiation, which can be used to distinguish these two phases. Considering both non-PVSK and PVSK phases are nonvolatile in moderate humidity (<40%) environment, the CsPbIBr<sub>2</sub> PM array can be potentially applied as a rewritable optical memory device. Figure S11 (Supporting Information) schematically illustrates the working mechanism of this application. The laser beam directly writes the individual PM pixels to transform the non-PVSK phase to PVSK phase, which represents the “write” or “set” process. The moisture exposure triggers the phase transition from the PVSK to non-PVSK phase again, which is the “erase” or “reset” process. Mapping of the pixels that have been written (set) can be obtained through reading the photocurrent of each PM pixel under a large-area white light irradiation (the “read” process). The PM pixel with a high photocurrent stores “1” and the pixel with a low photocurrent stores “0,” then the

optical information encoded by the laser beam writing can be restored.

We also characterized the set/reset cycle endurance and the data retention ability of the PM pixels. The photocurrents of the perovskite PM pixels over repetitive laser heating/moisture exposure cycles are presented in Figure 5a. The ratio of the photocurrent in the PVSK phase to that in the non-PVSK phase was observed to maintain above 50 over 10 cycles, which is high enough to distinguish the “1” state from the “0” state. The data retention capability was verified by recording the photocurrent continuously over time. As shown in Figure 5b, the photocurrents of the PM pixels in both phases remain relatively stable. No obvious degradation for the PVSK phase PM was observed after being stored for 7 d in ambient condition (20 °C, 30–40% humidity). The stability can be further improved by reducing the environment humidity during test. These findings show that the perovskite PM array can be used to conduct write-read-erase cycles many times, suggesting the potential of utilizing the nonvolatile phase-change properties of vapor-deposited CsPbIBr<sub>2</sub> for optical memory and information storage applications. For a complete cycle, the “write” process only took less than a second while the “erase” process usually cost longer time (20 min). Although the moisture exposure for reset process is not conventional for practical applications, the purpose of reset process is to erase the stored information, which is not frequently done for practical optical storage media.

## 2.5. Optical Information Storage in the PM Array

Herein, we use a  $8 \times 8$  PM pixel array to show the proof-of-concept demonstration of the optical information storage. Figure 6a shows the experimental setup. A prepatterned shadow mask with a number “19” was placed on top of the PM array, the NIR laser was scanned over the whole mask. The laser beam transmitted through the “19” number and transformed the phase of PM pixels under the image. The capability of the optical information storage was verified by reconstructing the projected optical pattern. After scan-measuring the photocurrent of each pixel, the photocurrent distribution of all 64 pixels was obtained. Each pixel

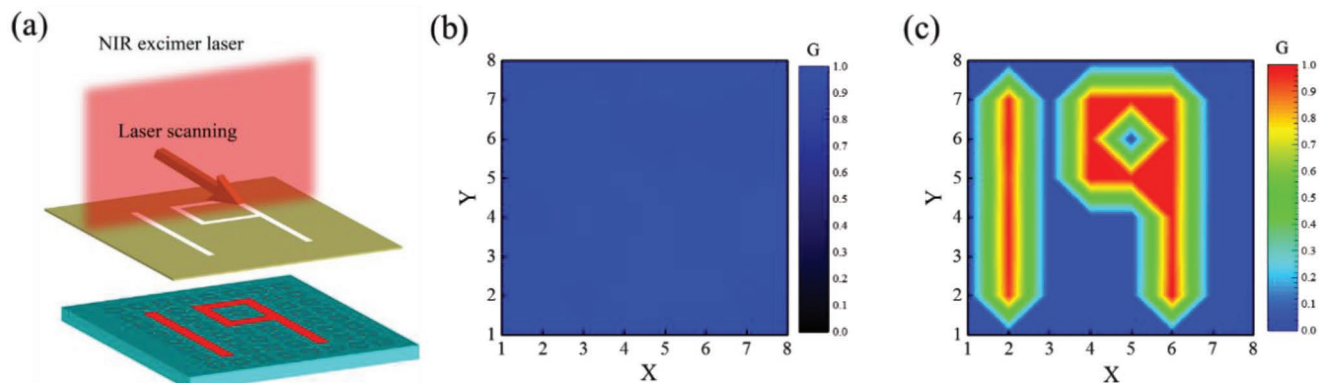


**Figure 6.** Optical information storage application of the flexible perovskite PM arrays. a) The schematic setup for storing optical information. The laser beam was scanned over the mask with an optical character, the optical image was retrieved by photocurrent mapping of all 64 pixels. b) The photocurrent mapping of non-PVSK phase PM array before laser scanning. c) A clear number “19” image reconstructed by mapping the photocurrent from each pixel after laser scanning.

is given a gray scale number ( $G$ ) between 0 and 1 based on the measured photocurrent ( $I_{\text{meas}}$ ) through the following equation<sup>[40]</sup>

$$G = \frac{I_{\text{meas}}}{I_{\text{max}}} \quad (2)$$

where  $I_{\text{max}}$  is the maximum light current of all 64 pixels. As shown in Figure 6b, the PM array in the non-PVSK phase shows uniform photocurrent mapping before laser scanning. After laser scanning through the “19” pattern, a clear number “19” image was retrieved through the photocurrent mapping as shown in Figure 6c. Our demonstrations open up the possibility of using vapor-deposited inorganic perovskite thin film for large-scale optical information storage devices.

### 3. Conclusions

In summary, we have demonstrated uniform inorganic perovskite films with excellent optoelectronic properties grown by a vapor-deposition process. The fabrication method can be easily implemented with various substrates. The reversible phase transitions between non-PVSK and PVSK phases were observed and confirmed by XRD. The two phases manifest significant differences in optical absorption, refractive index, and other optoelectronic properties. Utilizing the phase-change properties, the fabricated perovskite PM array can be applied as a rewritable optical memory device for optical information storage. The PM pixels exhibit good cycle endurance without performance degradation over ten cycles and great data retention capability in low-humidity ambient condition. These works suggest the versatile utilities of vapor-deposited inorganic perovskite films through the unique reversible phase-changing features and the potential application for large-scale optical storage devices.

### 4. Experimental Section

**Materials:** CsI (99.9% trace metal purity),  $\text{PbBr}_2$  (99.99% trace metal purity), and the Ag nanoparticle ink (Silverjet DGP-40LT-15C) for inkjet

printing were purchased from Sigma-Aldrich and used without further purification. The evaporation crucibles were purchased from Kurt J. Lesker.

**Inkjet Printing Ag Electrodes:** PET and glass substrates were first cleaned by ultrasonication with 2-propanol and deionized (DI) water in sequence. The Ag nanoparticle ink was loaded into the cartridge of an inkjet printer (Diamatrix), the cartridge was ultrasonicated briefly to reduce the aggregation of Ag nanoparticles. The voltage of printing nozzle was set at 23 V, the waveform frequency was set at 5 kHz. The cleaned substrates were well adhered to the printing platform using vacuum, the platform temperature was set at room temperature. The printing nozzle was controlled by the computer with the designed pattern to drop the Ag ink with a proper drop spacing distance (30  $\mu\text{m}$  for PET and 40  $\mu\text{m}$  for glass). The substrates were then heated in oven at 110  $^\circ\text{C}$  for 10 min to sinter the Ag electrodes.

**Perovskite Vapor Deposition:** Inorganic perovskite  $\text{CsPbI}_{1-x}\text{Br}_x$  was deposited by dual-source thermal deposition method. For  $\text{CsPbIBr}_2$  deposition, CsI and  $\text{PbBr}_2$  powder was placed into two crucibles separately. The vacuum chamber was pumped down to  $10^{-6}$  Torr. The evaporation rates of CsI and  $\text{PbBr}_2$  were 0.53 and 0.5  $\text{A s}^{-1}$  based on the calculation from their molecular mass and density. Two crucibles were heated simultaneously to appropriate temperature and the evaporation rates were monitored by two quartz crystal microbalances (QCMs) separately, the actual evaporation rates during the deposition process were controlled within 20% away from set values. Two QCMs were calibrated separately before deposition to determine the tooling factors for CsI and  $\text{PbBr}_2$ .

**Laser Direct Writing Process:** Laser heating was performed using a homemade system based on a Nd:YVO<sub>4</sub> 1064 nm laser source (Spectra Physics). The sample was placed on a XY translation stage, the laser beam was focused through a 10 $\times$  objective lens at the specific location of the sample. The photothermal effect on ITO or Ag layer induced by laser beam could increase the localized temperature and achieve the phase transition.

**Reversible Phase Transition of  $\text{CsPbIBr}_2$ :** The non-PVSK phase  $\text{CsPbIBr}_2$  film was heated on hotplate (160  $^\circ\text{C}$ ) for 10 min or by the 1064 nm laser beam to transform into the PVSK phase  $\text{CsPbIBr}_2$  film. To convert the PVSK phase to non-PVSK phase, the  $\text{CsPbIBr}_2$  film was placed in a humidity control box with relative humidity of 80% for 30 min. The reversible phase conversion process was carried out 20 times.

**Perovskite Thin Film Characterization:** The absorption spectra of perovskite films were acquired using a Varian Cary 5000 UV–vis–NIR Spectrophotometer. XRD patterns were obtained using Bruker D8 with a Cu K $\alpha$  radiation ( $\lambda = 1.54184 \text{ \AA}$ ). The surface morphology of perovskite films was measured by SEM (FEI Sirion) and AFM (Bruker Icon). The refractive index was measured using an ellipsometer (J. A. Woollam M2000), the raw data were fitted by the B-spline model on a Cauchy

dispersion glass substrate using Complete EASE software. Raman spectra were acquired by a Raman microscope (InVia, Renishaw), 785 nm laser was used as the excitation source to avoid the interruption of fluorescence from sample. The perovskite was deposited on the inkjet-printed Ag layer to enhance the Raman scattering intensity. The fluorescent images were obtained through a fluorescence microscope (EVOS, Thermo Fisher Scientific), the raw images were processed by ImageJ software to adjust the threshold intensity and remove background signal.

**Perovskite PM Array Measurement:** Current–voltage characteristics of perovskite PM pixels both in dark and under light illumination were measured by a source meter (Keithley 6430). The irradiation light was provided by a 405 nm laser source, the light intensity could be easily adjusted. The time-dependent current response was recorded under periodically on-off light illumination from a 405 nm laser source driven by the square wave from a signal generator. The spectral external quantum efficiency measurement was performed by using a tungsten-halogen light source to illuminate the device through a monochromator (Acton Research SpectraPro 275), which provides the monochromatic light excitation. The frequency response of the PM was measured by modulating the 405 nm laser light at different frequencies using an optical chopper. The generated photocurrent was recorded using a lock-in amplifier (Stanford Research SRS 830).

## Supporting Information

Supporting Information is available from the Wiley Online Library or from the author.

## Acknowledgements

This work was supported in part by National Science Foundation (Grant Nos. ECCS-1807397 and CHE-1836500). Part of the work was conducted at the Molecular Analysis Facility, a National Nanotechnology Coordinated Infrastructure site at the University of Washington which was supported in part by the National Science Foundation (Grant No. NNCI-1542101), the University of Washington, the Molecular Engineering and Sciences Institute, the Clean Energy Institute, and the National Institutes of Health. C.Z. would like to thank Felipe J. Pavinatto from the UW Clean Energy Institute Testbed (WCET) for discussion and help with inkjet printing.

## Conflict of Interest

The authors declare no conflict of interest.

## Keywords

inorganic perovskites, laser heating, optical information storage, phase change, photomemory, vapor-deposited perovskite

Received: April 2, 2019

Revised: May 3, 2019

Published online:

- [1] S. Abbas, M. Kumar, D.-K. Ban, J.-H. Yun, J. Kim, *ACS Appl. Electron. Mater.* **2019**.  
 [2] Y. Hu, J. Pérez-Mercader, *ACS Appl. Nano Mater.* **2018**, *1*, 3346.  
 [3] C. Qian, J. Sun, L.-A. Kong, Y. Fu, Y. Chen, J. Wang, S. Wang, H. Xie, H. Huang, J. Yang, Y. Gao, *ACS Photonics* **2017**, *4*, 2573.

- [4] Y. Zhai, J.-Q. Yang, Y. Zhou, J.-Y. Mao, Y. Ren, V. A. L. Roy, S.-T. Han, *Mater. Horiz.* **2018**, *5*, 641.  
 [5] M. Kim, H. Seong, S. Lee, H. Kwon, S. G. Im, H. Moon, S. Yoo, *Sci. Rep.* **2016**, *6*, 30536.  
 [6] B. R. Sutherland, E. H. Sargent, *Nat. Photonics* **2016**, *10*, 295.  
 [7] T. M. Brenner, D. A. Egger, L. Kronik, G. Hodes, D. Cahen, *Nat. Rev. Mater.* **2016**, *1*.  
 [8] A. Swarnkar, A. R. Marshall, E. M. Sanehira, B. D. Chernomordik, D. T. Moore, J. A. Christians, T. Chakrabarti, J. M. Luther, *Science* **2016**, *354*, 92.  
 [9] W. Wang, D. Zhao, F. Zhang, L. Li, M. Du, C. Wang, Y. Yu, Q. Huang, M. Zhang, L. Li, *Adv. Funct. Mater.* **2017**, *27*, 1703953.  
 [10] J. Miao, F. Zhang, *J. Mater. Chem. C* **2019**, *7*, 1741.  
 [11] L. Dou, Y. M. Yang, J. You, Z. Hong, W. H. Chang, G. Li, Y. Yang, *Nat. Commun.* **2014**, *5*, 5404.  
 [12] C. Zou, Y. Xi, C. Y. Huang, E. G. Keeler, T. Feng, S. Zhu, L. D. Pozzo, L. Y. Lin, *Adv. Opt. Mater.* **2018**, *6*, 1800324.  
 [13] J. Y. Chen, Y. C. Chiu, Y. T. Li, C. C. Chueh, W. C. Chen, *Adv. Mater.* **2017**, *29*, 1702217.  
 [14] E. Ercan, J. Y. Chen, C. C. Shih, C. C. Chueh, W. C. Chen, *Nanoscale* **2018**, *10*, 18869.  
 [15] J. Xue, D. Yang, B. Cai, X. Xu, J. Wang, H. Ma, X. Yu, G. Yuan, Y. Zou, J. Song, *Adv. Funct. Mater.* **2019**, 1807922.  
 [16] M. S. Kirschner, B. T. Diroll, P. Guo, S. M. Harvey, W. Helweh, N. C. Flanders, A. Brumberg, N. E. Watkins, A. A. Leonard, A. M. Evans, *Nat. Commun.* **2019**, *10*, 504.  
 [17] W. Fang, J. Yang, J. Gong, N. Zheng, *Adv. Funct. Mater.* **2012**, *22*, 842.  
 [18] J. Lin, M. L. Lai, L. T. Dou, C. S. Kley, H. Chen, F. Peng, J. L. Sun, D. L. Lu, S. A. Hawks, C. L. Xie, F. Cui, A. P. Alivisatos, D. T. Limmer, P. D. Yang, *Nat. Mater.* **2018**, *17*, 261.  
 [19] C. Y. Chen, H. Y. Lin, K. M. Chiang, W. L. Tsai, Y. C. Huang, C. S. Tsao, H. W. Lin, *Adv. Mater.* **2017**, *29*.  
 [20] G. Tong, H. Li, D. Li, Z. Zhu, E. Xu, G. Li, L. Yu, J. Xu, Y. Jiang, *Small* **2018**, *14*, 1702523.  
 [21] Y. Hu, Q. Wang, Y.-L. Shi, M. Li, L. Zhang, Z.-K. Wang, L.-S. Liao, *J. Mater. Chem. C* **2017**, *5*, 8144.  
 [22] E. M. Hutter, R. J. Sutton, S. Chandrashekar, M. Abdi-Jalebi, S. D. Stranks, H. J. Snaith, T. J. Sayenije, *ACS Energy Lett.* **2017**, *2*, 1901.  
 [23] M. Lai, Q. Kong, C. G. Bischak, Y. Yu, L. Dou, S. W. Eaton, N. S. Ginsberg, P. Yang, *Nano Res.* **2017**, *10*, 1107.  
 [24] J. Zheng, A. Khanolkar, P. Xu, S. Colburn, S. Deshmukh, J. Myers, J. Frantz, E. Pop, J. Hendrickson, J. Doylend, N. Boechler, A. Majumdar, *Opt. Mater. Express* **2018**, *8*, 1551.  
 [25] C.-H. Liu, J. Zheng, S. Colburn, T. Fryett, Y. Chen, X. Xu, A. Majumdar, *Nano Lett.* **2018**, *18*, 6961.  
 [26] G. Xu, N. Gao, C. Lu, W. Wang, Z. Ji, C. Bi, Z. Han, N. Lu, G. Yang, Y. Li, *Adv. Electron. Mater.* **2018**, *4*, 1700493.  
 [27] Q. Dong, Y. Fang, Y. Shao, P. Mulligan, J. Qiu, L. Cao, J. Huang, *Science* **2015**, *347*, 967.  
 [28] M. I. Saidaminov, A. L. Abdelhady, B. Murali, E. Alarousu, V. M. Burlakov, W. Peng, I. Dursun, L. F. Wang, Y. He, G. Maculan, A. Goriely, T. Wu, O. F. Mohammed, O. M. Bakr, *Nat. Commun.* **2015**, *6*, 7586.  
 [29] E. Mosconi, J. M. Azpiroz, F. De Angelis, *Chem. Mater.* **2015**, *27*, 4885.  
 [30] A. Mattoni, A. Filippetti, C. Caddeo, *J. Phys.: Condens. Matter* **2016**, *29*, 043001.  
 [31] S. S. Chou, B. S. Swartzentruber, M. T. Janish, K. C. Meyer, L. B. Biedermann, S. Okur, D. B. Burckel, C. B. Carter, B. Kaehr, *J. Phys. Chem. Lett.* **2016**, *7*, 3736.  
 [32] S. J. Kim, J. Byun, T. Jeon, H. M. Jin, H. R. Hong, S. O. Kim, *ACS Appl. Mater. Interfaces* **2018**, *10*, 2490.

- [33] J. A. Steele, H. F. Yuan, C. Y. X. Tan, M. Keshavarz, C. Steuwe, M. B. J. Roeffaers, J. Hofkens, *ACS Nano* **2017**, *11*, 8072.
- [34] I. Konidakis, T. Maksudov, E. Serpetzoglou, G. Kakavelakis, E. Kymakis, E. Stratakis, *ACS Appl. Energy Mater.* **2018**, *1*, 5101.
- [35] T. Jeon, H. M. Jin, S. H. Lee, J. M. Lee, H. I. Park, M. K. Kim, K. J. Lee, B. Shin, S. O. Kim, *ACS Nano* **2016**, *10*, 7907.
- [36] S. M. Jain, B. Philippe, E. M. Johansson, B.-W. Park, H. Rensmo, T. Edvinsson, G. Boschloo, *J. Mater. Chem. A* **2016**, *4*, 2630.
- [37] L. Q. Xie, T. Y. Zhang, L. Chen, N. Guo, Y. Wang, G. K. Liu, J. R. Wang, J. Z. Zhou, J. W. Yan, Y. X. Zhao, B. W. Mao, Z. Q. Tian, *Phys. Chem. Chem. Phys.* **2016**, *18*, 18112.
- [38] M. Ledinsky, P. Loper, B. Niesen, J. Holovsky, S. J. Moon, J. H. Yum, S. De Wolf, A. Fejfar, C. Ballif, *J. Phys. Chem. Lett.* **2015**, *6*, 401.
- [39] R. G. Niemann, A. G. Kontos, D. Palles, E. I. Kamitsos, A. Kaltzoglou, F. Brivio, P. Falaras, P. J. Cameron, *J. Phys. Chem. C* **2016**, *120*, 2509.
- [40] L. Gu, M. M. Tavakoli, D. Zhang, Q. Zhang, A. Waleed, Y. Xiao, K. H. Tsui, Y. Lin, L. Liao, J. Wang, *Adv. Mater.* **2016**, *28*, 9713.